Electron scattering mechanisms in fluorine-doped SnO_2 thin films

G. Rey' , C. Ternon, M. Modreanu, X. Mescot, V. Consonni, and D. Bellet

Citation: Journal of Applied Physics **114**, 183713 (2013); doi: 10.1063/1.4829672
View online: http://dx.doi.org/10.1063/1.4829672
View Table of Contents: http://aip.scitation.org/toc/jap/114/18
Published by the American Institute of Physics

Electron scattering mechanisms in fluorine-doped SnO_2 thin films

G. Rey,[1,a)] C. Ternon,[1,2] M. Modreanu,[3] X. Mescot,[4] V. Consonni,[1] and D. Bellet[1]
[1]*Laboratoire des Matériaux et du Génie Physique, CNRS—Grenoble INP, 3 parvis Louis Néel, 38016 Grenoble, France*
[2]*Laboratoire des Technologies de la Microélectronique, CNRS/UJF-Grenoble 1/CEA, 17 rue des Martyrs, 38054 Grenoble, France*
[3]*Micro-Nanoelectronics Centre, Tyndall National Institute, University College Cork, Lee Maltings, Dyke Parade, Cork, Ireland*
[4]*Institut de Microélectronique Electromagnétisme et Photonique-Laboratoire d'Hyperfréquences et de Caractérisation, Grenoble INP, 3 Parvis Louis Néel, 38016 Grenoble, France*

(Received 27 June 2013; accepted 23 October 2013; published online 14 November 2013)

Polycrystalline fluorine-doped SnO_2 (FTO) thin films have been grown by ultrasonic spray pyrolysis on glass substrate. By varying growth conditions, several FTO specimens have been deposited and the study of their structural, electrical, and optical properties has been carried out. By systematically investigating the mobility as a function of carrier density, grain size, and crystallite size, the contribution of each physical mechanism involved in the electron scattering has been derived. A thorough comparison of experimental data and calculations allows to disentangle these different mechanisms and to deduce their relative importance. In particular, the roles of extended structural defects such as grain or twin boundaries as revealed by electron microscopy or x-ray diffraction along with ionized impurities are discussed. As a consequence, based on the quantitative analysis presented here, an experimental methodology leading to the improvement of the electro-optical properties of FTO thin films is reported. FTO thin films assuming an electrical resistivity as low as $3.7 \cdot 10^{-4}\,\Omega\,\text{cm}$ (square sheet resistance of $8\,\Omega/\square$) while retaining good transmittance up to 86% (including substrate effect) in the visible range have been obtained.
 [http://dx.doi.org/10.1063/1.4829672]

I. INTRODUCTION

Transparent Conductive Oxide (TCO) films have been widely investigated and used in various devices, such as for instance solar cells, organic light emitting diodes, as well as for liquid crystal display panels.[1–4] The most successful and commonly used TCO is Indium Tin Oxide (ITO), but Indium is likely to become a commodity in short supply in the near future.[5] Among the other investigated materials, polycrystalline fluorine-doped SnO_2 (FTO) thin films have received increasing interest in recent decades due to their use in a wide variety of devices, such as gas sensors, coatings, oxidation catalysts, or solar cells.[6–8] In the field of photovoltaic, FTO thin films are used as front electrodes in solar cells and should be as transparent and conductive as possible. Until now, a low resistivity of a few $10^{-4}\ \Omega$ cm has been reached with a high mobility of about several tens of $\text{cm}^2\ \text{V}^{-1}\ \text{s}^{-1}$ and transmittance up to 90%.[1] FTO thin films are generally n-type materials and heavily doped with a charge carrier density larger than $10^{19}\,\text{cm}^{-3}$: as a result, FTO thin films are polycrystalline degenerate semiconductors. The Fermi level is located in the conduction band; and according to the Moss-Burstein effect, the optical bandgap energy is larger than 3.6 eV and strongly depends on the charge carrier density.[9,10]

In order to improve solar cell efficiency, one parameter that needs to be optimized is the carrier mobility within the TCO.[11,12] To further improve the carrier mobility of FTO thin films, a fundamental understanding of the electron scattering mechanisms is a prerequisite condition. Four different electron scattering mechanisms are reported to account for the electrical properties of TCO thin films: grain boundary (GB) scattering, phonon scattering, ionized impurity scattering, and twin boundary scattering.[13–17]

In the former case, the contribution of the grain boundaries, which assume a disordered nature with a large number of defects originating from dangling bonds, is taken into account. This results in the formation of trapping states in the bandgap that are electrically charged, leading to the occurrence of intergrain band bending and potential energy barriers at grain boundaries that constitute barriers for the transport of free charge carriers. The mobility dependence on the potential energy barrier was reported early by Petritz.[18] It was stated in the approaches described, respectively, by Seto *et al.*[19] and Bruneaux *et al.*[20] that the potential barrier height depends on the charge carrier density and can be overcome by thermo-ionic emission or tunneling effects. For charge carrier densities lower than $10^{20}\,\text{cm}^{-3}$, it is expected that the mobility and resistivity are mainly driven by grain boundary scattering.

However, for charge carrier density higher than $10^{20}\,\text{cm}^{-3}$, ionized impurities can act as scattering centers and thus directly interact with free charge carriers according to Coulomb interaction. Conwell and Weisskopf[21] derived the mobility dependence on the charge carrier density in a truncated Coulomb potential while Brooks[22] introduced a screened Coulomb potential. Dingle[23] considered the case of

a)Author to whom correspondence should be addressed. Electronic mail: germrey@gmail.com

degenerate semiconductors, which is highly relevant for FTO thin films. Pisarkiewicz *et al.*[24] eventually took into account the non-parabolicity of the conduction band for FTO thin films. Generally, it is expected that the mobility decreases when free charge carrier density is increased.

Grain boundary scattering and ionized impurity scattering mechanisms have also been investigated in other TCO materials such as Ga-doped ZnO or ITO films and are often supposed to be the major scatterings.[25,26] Besides, a process of twin boundary scattering is shown to play a role. Indeed, as discussed in this paper, the presence of a high density of lamellar twins in FTO can contribute to lower the observed electro-optical properties of FTO as compared with other TCOs.

In this work, the carrier mobility has been measured for FTO films grown under different experimental conditions. For each studied sample, the structural, electrical, and optical properties of FTO thin films are investigated by scanning and transmission electron microscopy imaging, x-ray diffraction (XRD), Hall Effect measurements, transmittance and reflectance (T&R) spectrophotometry, as well as spectroscopic ellipsometry (SE). An in-depth analysis of the relationship between the structural, optical, and transport properties enables to quantitatively estimate the contribution of each of the carrier scattering mechanisms, which vary with growth conditions. We also should outline that such investigation requires the determination of the effective mass, which is a key parameter for describing carrier transport in materials.

II. EXPERIMENTAL PROCEDURE

A. Deposition technique

Polycrystalline FTO thin films were grown by ultrasonic spray pyrolysis on a Corning C1737 borosilicate glass substrate. The growth temperature was varied in the range of 360 to 480 °C. The chemical precursor solution was composed of 0.16 M of $SnCl_4 \cdot 5H_2O$ and x M of NH_4F in a methanolic solution with x varying in the range from 0 to 0.28 M. The sprayed precursor solution volume and flow rate were varied in the ranges of 2 to 40 ml and 0.5 to 2 ml min^{-1}, respectively. The combination of all of these experimental parameters leads to FTO specimens with controlled charge carrier densities, grain sizes, and film thickness.[27]

B. Characterization

Field-emission scanning electron microscopy (FESEM) imaging was recorded with a ZEISS Ultra Plus microscope. Top-view FESEM images were processed using ImageJ in order to deduce the surface area of each grain. The size of a grain was defined as the square root of its grain surface area. Cross-sectional high resolution transmission electron microscopy (HRTEM) specimens were prepared by mechanical lapping and polishing followed by argon ion beam milling according to standard techniques. HRTEM images were recorded with a JEOL JEM-2010 microscope operating at 200 kV.

XRD patterns were collected with a Bruker D8 Advance diffractometer using CuKα_1 radiation according to the Bragg-Brentano configuration. The θ-2θ XRD measurements were performed between 20° and 70° (in 2-Theta scale).

Hall effect measurements were performed at room temperature using a homemade setup operating under a magnetic field of 0.5 T in the classical Van der Paw configuration.

Fluorine concentrations were measured by proton induced gamma ray emissions and results are reported by Ferrer *et al.*[28]

Dielectric function of FTO thin films were measured either by SE or T&R spectrophotometry. SE measurements were performed at room temperature with three different angles of incidence (56°, 63°, and 70°) and using a rotating compensator ellipsometer with CCD array detection (Woollam M2000). Before any SE measurements, the glass substrate backside was mechanically roughened using sand paper in order to suppress the influence of backside reflection. A simple optical model was used in the SE analysis where the FTO layer is composed of two layers: a perfect FTO layer plus a roughness layer. For the SE analysis using the optical model, dielectric functions (or optical constants) of each layer are required. The optical constants of the glass substrate were obtained from the SE analysis of the glass substrate and were expressed by the Sellmeier model.[29] The dielectric function of highly doped TCO layers can be modeled from the combination of the Tauc-Lorentz[30] and Drude models.[31,32]

Normal incidence transmittance and near-normal incidence reflectance (at 8°) spectra were recorded between 250 and 2500 nm using a spectrophotometer (Perkin-Elmer Lambda 950). T&R data analysis was performed to calculate the refractive index with the help of a graphical inversion method.[27] Both experimental methods (SE and T&R) lead to very similar results in terms of dielectric functions.

III. RESULTS AND DISCUSSION

A. Structural properties

The structural morphology of FTO thin films is presented through the FESEM and HRTEM images of Figure 1. Typically, FTO thin films are polycrystalline: a general feature always observed for the most common crystalline TCOs. The grain preferred orientation strongly depends on the FTO growth conditions: still, the ⟨110⟩, ⟨100⟩, and ⟨301⟩ crystallographic directions are generally dominant.[33,34]

A more specific characteristic of FTO concerns the presence of slightly textured sub-micrograins. Figure 1 clearly reveals the presence of planar extended defects (twins) crossing the entire grains. Moreover, their density is high as several extended defects can be observed within one grain. These extended defects can be identified by HRTEM imaging as {101} twin planes, in agreement with Refs. 20, 34, and 35. As a consequence, it is important to distinguish between grain size and crystallite size, the latter corresponding to the small coherent domains between two twin boundaries. In this study, the grain size (L_g) is determined from statistical analysis of top view FESEM images and defined as mean value of grain size weighted by the grain surface area (this definition is more relevant for transport properties analysis as larger grains show larger section). While the

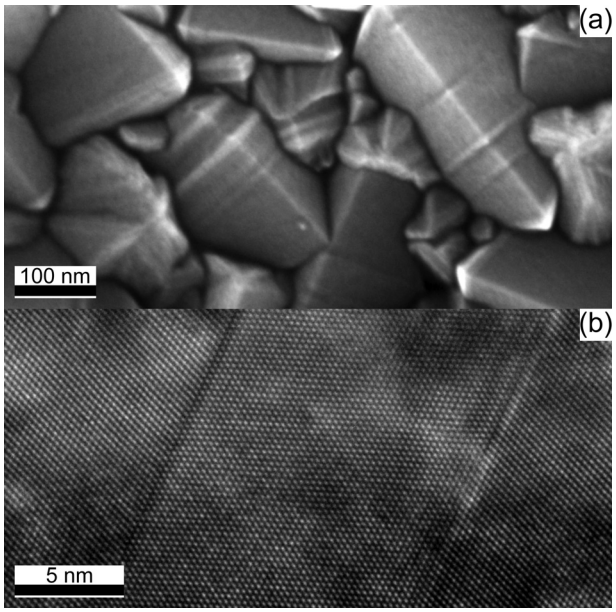

FIG. 1. (a) Top-view FESEM image of FTO thin film showing the presence of grains as well as lamellar twins within grains. (b) Cross-section TEM image of FTO thin films revealing the presence of {101} lamellar twins within grains.

crystallite size (L_c) is associated with the coherent crystal length and is deduced from XRD patterns by using the Scherrer equation

$$\Delta(2\theta) = K\frac{\lambda}{L_c \cos\theta}, \quad (1)$$

where θ is the Bragg angle, $\Delta(2\theta)$ the Bragg peak width, λ the x-ray wavelength and K a correcting coefficient depending on experimental setup and crystallite shape and considered equal to 1 in the present case. We will assume in this work that the different crystallites will scatter x-ray in a non coherent way; and for the sake of simplicity; we will relate directly the coherent length to the average crystallite size.

Figure 2 reports L_c for several Bragg peaks by using the Scherrer relation and L_g calculated from FESEM top view analysis as a function of film thickness controlled by the sprayed solution volume, all other parameters kept constant.[27,33] As expected, the crystallite size is systematically much smaller than the grain size and the thicker the FTO film is, the larger both the grain size and crystallite size are (see Figure 2). This is consistent with grain growth observed in polycrystals where both normal and abnormal grain growths take place.[36] Applied to FTO films, these normal and abnormal grain growths processes depend on several film characteristics and especially upon film thickness and growth temperature.[33,34]

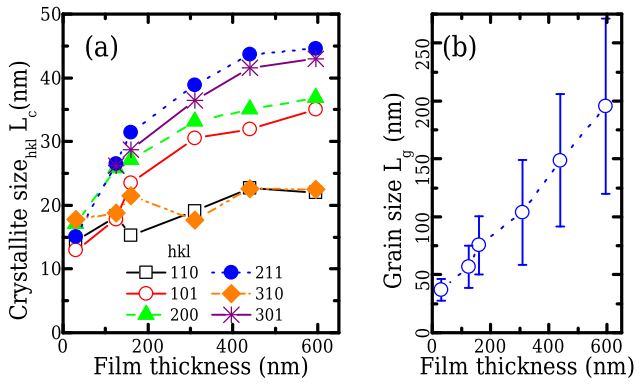

FIG. 2. (a) Crystallite sizes associated with various crystallographic orientations (hkl) versus film thickness of FTO specimens. Crystallite sizes were estimated from X-Ray diffraction data by using the Scherrer equation (Eq. (1)). (b) Grain size determined by FESEM versus FTO sample thickness (error bars showing standard deviation of the grain size distribution).

B. Electrical properties

The electrical properties of FTO thin films are reported in Figure 3 as a function of film thickness. For this specimen series, only the sprayed volume was varied (from 2 to 40 ml) while all of the other process parameters were kept fixed. Therefore, it is not surprising to observe that the carrier density is not thickness dependent. The carrier mobility, deduced from Hall measurements, increases with film thickness. Qualitatively, this can be associated with an improvement in the crystalline quality: thicker specimens exhibit larger grains and crystallites (see Figure 2),[33] which lower electron scattering originating from extended structural defects. A quantitative approach will be presented in Sec. III D where all of the electron scattering mechanisms will be discussed and calculated. As a consequence of increasing electron mobility and having a constant carrier density for thicker specimen, a decrease in electrical resistivity is observed. Values of $3.7 \times 10^{-4}\,\Omega\,\text{cm}$ can be measured associated with optical transmittance up to 86% in the visible range, corresponding to a Haacke's figure of merit[37] in the range of $27.7 \times 10^{-3}\ \Omega^{-1}$ and can be considered to properties close to the state of the art for FTO specimen when compared with literature.[1,38]

C. Dielectric function and free carrier model

In the spectral range of relevant electromagnetic wavelengths for the applications in which TCOs are used (i.e., solar cells, flat screens, etc.), free electrons dominate the electrical and optical properties. These properties can be

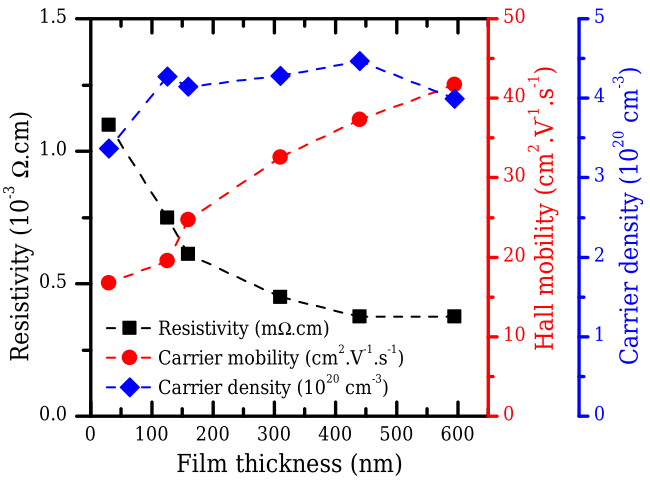

FIG. 3. Evolution of the electrical resistivity, Hall mobility, and carrier density of the FTO films deposited on glass substrate versus film thickness.

described by the Drude free electron theory.[39] This latter theory often accounts for the measurable properties of TCOs, such as transmittance and reflectance, and their relationship to extrinsically controllable parameters (such as carrier concentration) and intrinsic uncontrollable properties (such as crystal lattice and effective mass).

If one assumes that electrons can freely move between two successive scattering events, the equation of motion can subsequently be solved by considering the effect of an electric field.[39] Therefore, the dielectric function of the material can be written as follow:

$$\varepsilon(\omega) = \varepsilon_\infty \left(1 - \frac{{\omega_P}^2}{\omega^2 + j\frac{\omega}{\tau}}\right), \tag{2}$$

where ε_∞ is the value of the dielectric constant at high frequencies, τ is the average time between two successive electron scatterings, and ω_P is called the plasma pulsation and corresponds to the collective oscillations of the free carriers of density n_c

$$\omega_P = \sqrt{\frac{n_c e^2}{m^* \varepsilon_0 \varepsilon_\infty}}, \tag{3}$$

where m^* is the carrier effective mass, ε_0 is the vacuum permittivity, and e is the elementary charge.

Therefore, the dielectric function $\varepsilon(\omega)$ can be described with only three parameters: ε_∞,ω_P, and τ. The experimental dependence of ε versus energy is reported in Figure 4(a) for samples associated with three different carrier densities. The dashed lines represent the best fits obtained using Eq. (2). The good agreement between experimental data and the fits proves that the Drude model describes well the dielectric function behavior of FTO specimen. Small deviations are observed for the lowest wavelengths where interband transitions occur. However, the obtained values, reported in Table I, for $\varepsilon_\infty, \omega_P$, and τ are in good agreement with data obtained from the literature.[40]

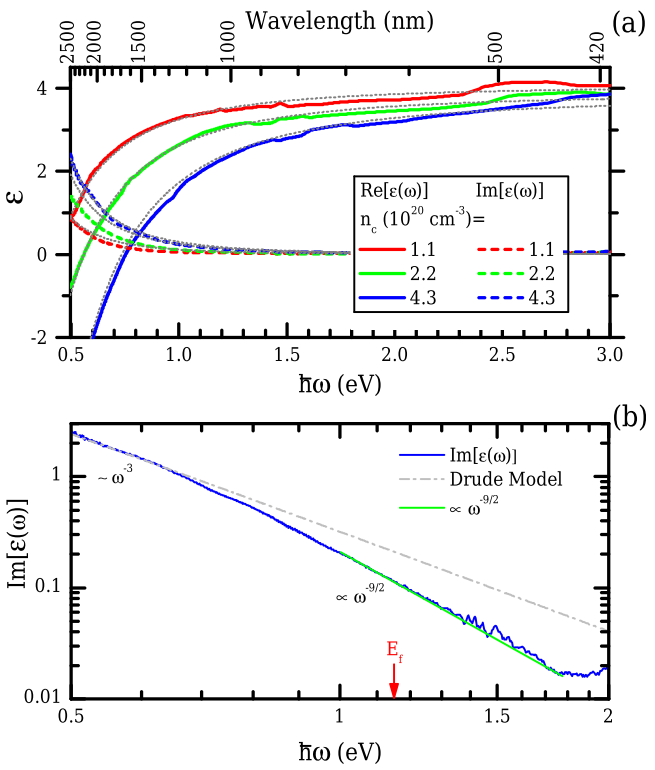

FIG. 4. (a) Real (continuous lines) and imaginary (dashed lines) parts of the dielectric constant of FTO versus energy for different carrier concentrations. The grey dotted curves correspond to the best fit by considering the Drude model (see Eq. (2)). (b) Imaginary part of the dielectric constant of highly doped FTO film ($n_c = 4.1 \times 10^{20}\,\mathrm{cm}^{-3}$). The dotted-dashed line shows fit using the Drude model associated with a ω^{-3} behavior at low frequencies. In the high frequency range, line shows the $\omega^{-9/2}$ dependence, which refers to ionized impurity scattering (see text).

D. Electron scattering mechanisms

1. Generalities

In this section, we consider approaches that enable us to quantitatively estimate which are the dominant carrier scattering mechanisms in the FTO films under investigation.

The two main scattering processes playing a dominant role in TCOs are: grain boundary scattering and ingrain scattering. The later refers to ionized impurity scattering and to a lower extent to phonons.[13,25,26] Single crystalline samples generally exhibit higher mobility than their polycrystalline variant, especially for low charge carrier densities, indicating that grain boundary scattering can be important.[1] However, the GB scattering dominance is still a question of debate.[41] The dominance of these scattering processes varies with electron concentration as well as with chemical compounds or with structural properties of the considered TCO thin film. In the case of electron concentration higher than $10^{20}\,\mathrm{cm}^{-3}$, the dominant scattering is often inferred to be ingrain scattering.[42,43]

In order to at least partially disentangle the effects of ingrain and GB scattering on electron transport in TCOs, a frequent approach consists in measuring the electron mobility in two different ways.[2,25,32,44,45] The Hall measurements describe the mobility of electrons (μ_{Hall}), which are moving across many grains and grain boundaries in the conduction path. μ_{Hall} is then limited by both scattering processes within

TABLE I. Experimental values of carrier density n_c deduced from Hall effect measurements, plasma angular frequency ω_P, high frequency dielectric constant ε_∞, and the mean time between two consecutive scattering events of free carrier τ extracted from the fit of the dielectric function of FTO layers (Fig. 4(a)) using Eq. (2). The effective mass m^* is calculated from the values of n_c, ω_P, ε_∞, and τ with the help of Eq. (3).

n_c ($10^{20}\,\mathrm{cm}^{-3}$)	$\hbar \cdot \omega_p$(eV)	ε_∞	τ (10^{-15} s)	m^* (m_e)
0.2	0.22	4.1	3.9	0.14
0.9	0.44	4.1	4.5	0.16
1.1	0.45	4.1	5.5	0.18
2.2	0.58	3.9	4.7	0.23
3.8	0.74	3.8	5.6	0.25
4.0	0.74	4.0	4.7	0.25
4.2	0.77	4.0	4.8	0.24
4.3	0.77	4.1	4.6	0.24
4.3	0.74	3.9	5.1	0.28
4.3	0.76	3.8	4.8	0.27
4.5	0.75	3.7	5.3	0.29

the grains and at GBs. On the contrary, the optical mobility (μ_{opt}), deduced from the analysis of free electrons in the framework of the Drude model theory, is only related to ingrain scatterings since the oscillation amplitude of carriers driven by the electromagnetic waves is much smaller than the size of the sub-structure delineated by extended defects in the present experimental conditions. By comparing μ_{Hall} and μ_{opt}, the contribution of GB scattering on electron mobility can then be estimated, as shown below.

In addition to the main scattering mechanisms presented above, twin boundaries which are observed in FTO specimens, can also play a role in the carrier scattering, as discussed below.[35]

2. Determination of the effective mass and optical mobility

According to the Drude model theory, the optical mobility can be calculated using the following equation:

$$\mu_{opt} = \frac{e\tau}{m^*}. \tag{4}$$

Thanks to the analysis of the frequency dependence of $\varepsilon(\omega)$ (reported in Figure 4(a)) combined with Eq. (3), m^* is determined and reported in Table I and in Figure 5(a) as a function of the carrier density n_c. The values are in agreement with those reported in the literature for FTO.[9,46] The increase of m^* versus n_c indicates that the FTO conduction band has a non parabolic dispersion relation. Indeed, for degenerated semiconductors, the energy wave-vector relation is no longer parabolic. The effective mass can then be expressed following:[24,46]

$$m^* = m_0{}^*.\sqrt{1 + \frac{2.\varsigma.\hbar^2}{m_0{}^*}.(3.\pi^2.n_c)^{2/3}}, \tag{5}$$

where ς is called the non-parabolicity constant of the conduction band and $m_0{}^*$ is the effective mass at the bottom of the conduction band. The best fit of $m^*(n_c)$ is reported as a solid line in Figure 5(a). From this fit, $m_0{}^*$ and ς are determined as $0.09\,m_e$ and $0.8\,\mathrm{eV}^{-1}$, respectively. These values are in good agreement with those reported in the literature: $0.094\,m_e$ and $1.035\,\mathrm{eV}^{-1}$.[46] This analysis shows that in the case of degenerated FTO, the dependence of the effective mass versus the carrier density should be considered. The m^* values can vary by a factor of two in the n_c value range considered here.

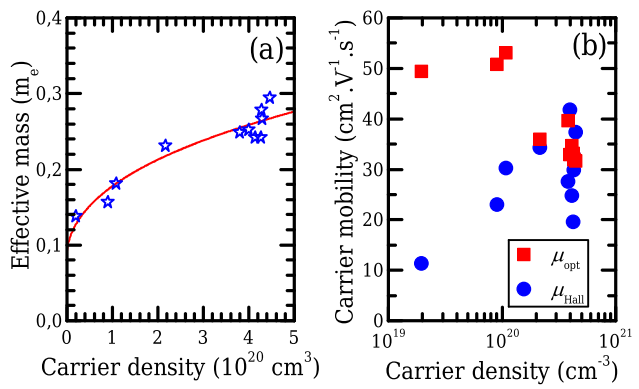

FIG. 5. (a) Carrier effective mass curves versus free carrier density. The continuous curve represents the best fit of the data using Eq. (5). (b) Optical (μ_{opt}) and Hall (μ_{Hall}) carrier mobility in FTO specimen versus carrier density.

Finally, Figure 5(b) reports both Hall and optical carrier mobility versus the carrier density. As discussed earlier, μ_{opt} is only associated with the scattering events occurring within crystallites, while μ_{Hall} takes into account scattering effects originating from grain boundaries or twins as well.

For lightly doped FTO specimens (i.e., $n_c < 10^{20}\,\mathrm{cm}^{-3}$), μ_{opt} is significantly larger than μ_{Hall}. This is an indication that, for the slightly doped FTO thin films, twins and GBs have a large contribution on the carrier scattering: this is due to the occurrence of potential barriers at extended defects, limiting the mobility.

For highly doped FTO specimens, μ_{opt} and μ_{Hall} have rather similar values; this would indicate that the main scattering mechanism would be ingrain scattering. However, this is not valid for all highly doped specimens as some of them show a much higher μ_{opt} than μ_{Hall} and an in depth study has to be considered to identify the contribution of each mechanism, as shown below. The fact that μ_{opt} could even be slightly lower than μ_{Hall} does not have any physical meaning and might rather arise from experimental uncertainties, especially for the thicker FTO samples, where the roughness is not taken into account for data extraction.

3. Ingrain scattering effects on electron mobility

Ingrain scattering effects are often dominated by ionized impurities and the associated mobility is denoted μ_{ii}. To a less extent, the scattering from neutral impurities should also be considered and the associated mobility is denoted μ_n. Finally, one should also take into account the electron scattering by phonons to which is attached the mobility μ_{ph}. By assuming that these three scattering mechanisms are independent, the Matthiessen law can be used for calculating the ingrain mobility μ_{cr}

$$\frac{1}{\mu_{cr}} = \frac{1}{\mu_{ii}} + \frac{1}{\mu_n} + \frac{1}{\mu_{ph}}. \tag{6}$$

The expression of μ_{ii} can be computed for degenerate semiconductors by taking into account the non-parabolicity of the conduction band[24,26]

$$\mu_{ii} = \frac{3(\varepsilon_r\varepsilon_0)^2.h^3}{m^{*2}e^3}\frac{1}{F}\frac{n_c}{Z_{ii}^2.N_{ii}}, \tag{7}$$

$$F = \left\{1 + \frac{4\xi_{np}}{\xi_d}\left(1 - \frac{\xi_{np}}{8}\right)\right\}\ln(1+\xi_d) - \frac{\xi_d}{1+\xi_d} - 2\xi_{np}\left(1 - \frac{5\xi_{np}}{16}\right), \tag{7a}$$

$$\xi_d = (3\pi^2)^{1/3}\frac{\varepsilon_r\varepsilon_0 h^2}{e^2}\frac{n_c^{1/3}}{m^*}, \tag{7b}$$

$$\xi_{np} = 1 - \frac{m_0^*}{m^*}, \tag{7c}$$

where ε_r is the relative dielectric constant, Z_{ii} and N_{ii} are respectively the charge (in elementary charge unit) and the concentration of ionized impurities.

As reported elsewhere,[27] μ_n can be neglected, in agreement with conclusions from similar works on ZnO or ITO.[26]

The carrier scattering by phonons can be estimated by using the mobility data measured for SnO_2 single crystals with a low doping concentration ($n_c = 8.5 \times 10^{15}\,cm^{-3}$).[47] A phonon mobility value of 260 $cm^2\,V^{-1}\,s^{-1}$ at room temperature was reported,[47] which is much higher than the experimental mobility of polycrystalline FTO thin films as reported in Figure 3. Therefore, the ingrain contribution to the mobility should be mainly dominated by ionized impurity scattering and to a much lower extent by phonon scattering. An assessment of this conclusion can be provided by analyzing the frequency dependence of the imaginary part of the dielectric function $Im(\varepsilon(\omega))$ as reported Figure 4(b). Different behaviors are expected, depending on the relative values of E_F and $\hbar.\omega$. For each sample, using the previous obtained values of each parameter, the Fermi energy can be expressed from the bottom of the conduction band by[24,46]

$$E_F = \frac{1}{2.\varsigma}.\left(\sqrt{1+\frac{2.\varsigma.\hbar^2}{m_0{}^*}.(3.\pi^2.n_c)^{2/3}}-1\right). \quad (8)$$

According to the literature, for photon energy lower than the Fermi level E_F ($\hbar.\omega \ll E_F$), $\varepsilon(\omega)$ is well described by the Drude model.[48] While for photon energy higher than the Fermi energy E_F, $Im(\varepsilon(\omega))$ variation with ω depends on scattering mechanisms. If $\omega^2.\tau^2 \gg 1$, then the dependencies of $Im(\varepsilon(\omega))$ can be considered as followed:[49]

→ If $\hbar.\omega \ll E_F$: $\mathrm{Im}(\varepsilon(\omega)) \propto \omega^{-3}$ following the Drude model
→ If $\hbar.\omega \geq E_F$: $\mathrm{Im}(\varepsilon(\omega)) \propto \omega^{-5/2}$ for acoustic phonon scattering
$\propto \omega^{-7/2}$ for optical phonon scattering
$\propto \omega^{-9/2}$ for ionized impurity scattering.

Figure 4(b) exhibits the ω dependence of $Im(\varepsilon(\omega))$ showing the Drude's dependency for low ω value ($\hbar\omega \ll E_F$) and a dependency with $\omega^{-9/2}$ for the higher ω value range ($\hbar.\omega \geq E_F$). This observation confirms that ionized impurity scattering is the dominant mechanism for the ingrain mobility.

Finally, by taking into account the uncertainty of the fluorine concentration that was measured by proton induced gamma ray emissions,[28] this leads to a mobility μ_{cr} value in the range of 37 to 53 $cm^2\,V^{-1}\,s^{-1}$ calculated with the help of Eqs. (6) and (7).[27]

4. Effects of extended defects on electron mobility

As shown in Figure 5(b), the mobility μ_{Hall} does not follow the dependence for ionized impurity scattering for highly doped samples ($2 \times 10^{20}\,cm^{-3} < n_c < 4.6 \times 10^{20}\,cm^{-3}$). Figure 6 exhibits the plot of the experimental Hall mobility of electrons in highly doped FTO versus crystallite and grain size deduced from XRD and FESEM analysis, respectively. The experimental L_c values have been determined by

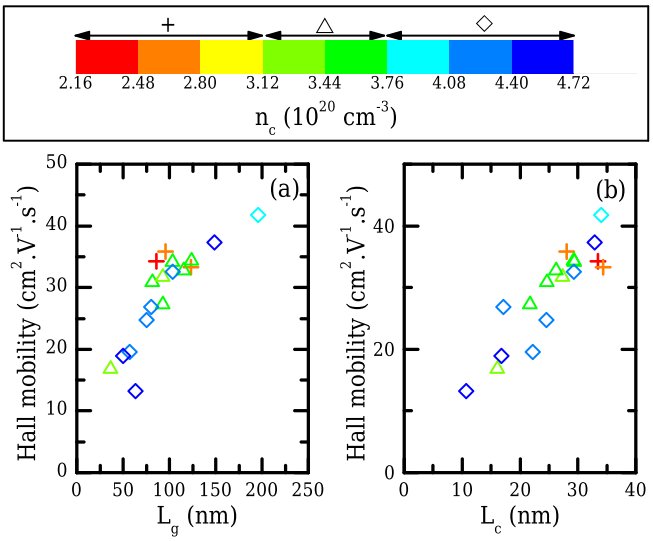

FIG. 6. (a) Evolution of Hall mobility versus grain size (L_g). (b) Evolution of Hall mobility versus averaged crystallite size (L_c). Data are shown with a color and shape-carrier density correspondence.

considering the average crystallite size values as reported in Figure 2(a) for the six considered XRD Bragg peaks: (110), (101), (200), (211), (310), and (301). For both cases, it should be noted that the mobility follows a rather linear dependence. Such a linear dependence between carrier mobility and grain size has already been reported in the literature for Ga-doped ZnO layers grown by molecular beam epitaxy.[16] Although the dependence of μ_{Hall} versus L_c or L_g is clearly shown in Figure 6, it is not possible to conclude on the limiting mechanism between grain, twin boundary scattering, or ingrain scattering since the contribution of the two first scattering mechanisms have not yet been disentangled. Therefore, grain boundary effects on electron mobility will be discussed in Sec. III D 4 a while the effects of twin boundaries will be discussed in Sec. III D 4 b.

a. Grain boundary effects on electron mobility. Grain boundaries lead to electronic defects in the semiconductor band gap. These defect levels are charged by carriers from grains and are attributed to dangling bonds of ions situated at the border of the grains. Charge balance causes a depletion zone on each side of a grain barrier, which leads to an energetic barrier of height ϕ_b for the carriers.[19] Carriers should cross this barrier either by tunnel effect or by thermo-ionic emission. For degenerate semiconductors, the Fermi level can be higher than the barrier height ϕ_b. The mobility associated with the presence of grain boundaries can be calculated through the following equation:[14,50]

$$\mu_{GB} = \gamma_{eff}\frac{4\pi m^* e}{h^3}\frac{\Lambda}{\Lambda+\frac{3}{4}w_b}\frac{L_g}{n_c}k_BT\ln\left\{1+\exp\left[\frac{-(\phi_b-E_F)}{k_BT}\right]\right\}, \quad (9)$$

where γ_{eff} is a correcting factor ranging from 0 to 1.[14] L_g is the average distance between neighboring GBs and can be associated in a first approximation with the grain size deduced from FESEM analysis, Λ is the mean free path of carriers within grains and finally w_b is the GB potential barrier width.

Note that γ_{eff} is associated with the non-homogeneity of the current density flowing through the material. This is attributed to grain size distribution as well as to the variations of the chemical composition at GBs as explained in details by Prins *et al.* in Ref. 14. The mean free path for a degenerated semiconductor can be estimated through the following equation:[39]

$$\Lambda = \frac{\mu_{cr}}{e}\sqrt{2m^*E_F}. \tag{10}$$

Using the depletion approximation, w_b and ϕ_b can be expressed as follow:[19]

$$w_b = \frac{Q_t}{N_d} \quad \text{and} \quad \phi_b = \frac{e^2Q_t^2}{8\varepsilon_r\varepsilon_0 N_d}, \tag{11}$$

where Q_t is surface density of electron traps at the grain boundary, which is reported at $4\times10^{12}\,\text{cm}^{-2}$ in case of FTO.[20] N_d is the density of electron donor impurities.

Therefore, the contribution of grain boundaries to electron scattering can then be calculated using Eqs. (9)–(11) as follows:

$$\mu_{GB}(cm^2.V^{-1}.s^{-1}) \cong 5.8\gamma_{eff}L_g(nm)\left(n_c(nm^{-3})\right)^{-1/4}, \tag{12}$$

only valid for the highly doped sample showing $2\times10^{20}\,\text{cm}^{-3}<n_c<4.6\times10^{20}\,\text{cm}^{-3}$. The only remaining unknown parameter is γ_{eff}. It will be considered as one of only two free parameters when the total electron mobility will be calculated in Sec. III D 5.

b. Twin boundary effects on electron mobility. The influence of defects, such as twins, has already been considered in the literature for the highly doped semiconductors. When the average distance between such defects is known (supposed here to be equal to L_c), their contribution to the electron mobility μ_{twin} can then be calculated by[51]

$$\mu_{twin} = \frac{e}{\pi h}\frac{L_c}{n_c}\int_0^{k_F}\frac{k}{r(k)}dk, \tag{13}$$

where $r(k)$ is the probability of scattering an electron having a wave vector k. k_F is the Fermi wave vector which dependence with n_c should consider the non-parabolicity of the conduction band as discussed above and is deduced from the Fermi energy (Eq. (8)) and from the non parabolic dispersion relation: $\hbar^2k^2 = 2m_0^*(E+\xi.E^2)$. By assuming that r does not depend on k, Eq. (13) then leads to

$$\mu_{twin} = \frac{e}{\pi h}\frac{L_c}{n_c}\frac{k_F^2}{2r}. \tag{14}$$

Using a value 0.5 for r,[52] one can then deduce the following expression for μ_{twin} (only valid for the highly doped samples with $2\times10^{20}\,\text{cm}^{-3}<n_c<4.6\times10^{20}\,\text{cm}^{-3}$):

$$\mu_{twin}(cm^2.V^{-1}.s^{-1}) \cong 7.4\,L_c(nm)\left(n_c(nm^{-3})\right)^{-1/3}. \tag{15}$$

5. Total electron mobility

The influence of each of the different scattering mechanisms has been discussed and quantified in the previous sections. Hence, numerical values of the twin contribution of the electron mobility μ_{twin} (Eq. (15)) associated with μ_{GB} (Eq. (12)) and μ_{cr} (see Sec. III D 3) will be used to disentangle the relative contribution of each scattering mechanism to the total electron mobility for highly doped samples ($2\times10^{20}\,\text{cm}^{-3}<n_c<4.6\times10^{20}\,\text{cm}^{-3}$). The global electron mobility, μ, can now be expressed as follows:

$$\mu^{-1} = {\mu_{cr}}^{-1} + {\mu_{GB}}^{-1} + {\mu_{twin}}^{-1}, \tag{16}$$

$$\text{With:}\quad \mu_{cr} \in (\text{Refs. 37 and 53}), \tag{16a}$$

$$\mu_{GB} \cong 5.8\gamma_{eff}L_g{n_c}^{-1/4}, \tag{16b}$$

$$\mu_{twin} \cong 7.4L_c{n_c}^{-1/3}, \tag{16c}$$

where mobilities are expressed in $\text{cm}^2\ \text{V}^{-1}\ \text{s}^{-1}$, L_g and L_c in nm and n_c in nm^{-3}. The only two unknown parameters are γ_{eff} and μ_{cr}. We assume that γ_{eff} and μ_{cr} are the same for all samples since the considered doping range is narrow ($2\times10^{20}\,\text{cm}^{-3} < \text{n}_\text{c} < 4.6\times10^{20}\,\text{cm}^{-3}$). The best fit obtained using Eq. (16) is reported in Figure 7(a) by using the following values: $\gamma_{eff} = 0.13 \pm 0.02$ and $\mu_{cr} = 53 \pm 1\,\text{cm}^2\ \text{V}^{-1}\ \text{s}^{-1}$. Since $\mu_{GB} \propto L_g{n_c}^{-1/4}$ and $\mu_{twin} \propto L_c{n_c}^{-1/3}$, the calculated total electron mobility values are plotted in the

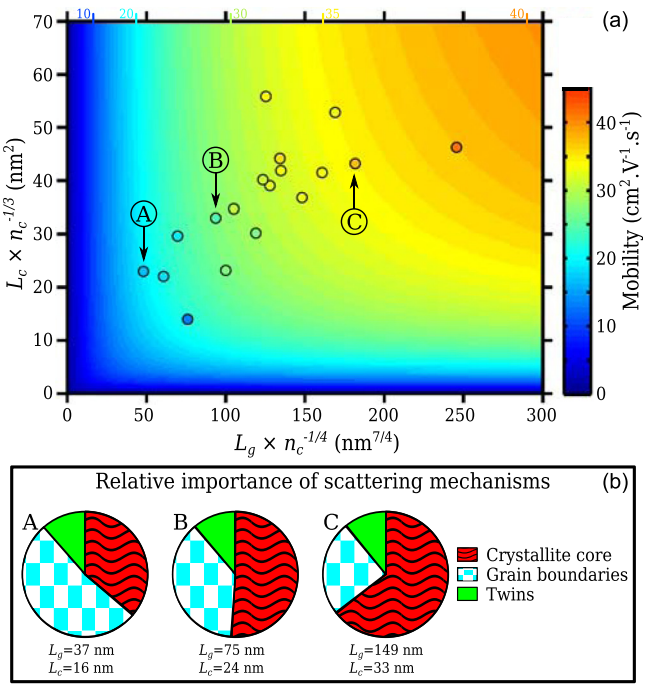

FIG. 7. (a) Calculated values of the free carrier mobility for highly doped FTO specimen ($n_c \approx 2$–$4.7\times10^{20}\,\text{cm}^{-3}$) using Eq. (16) when considering $\gamma_{eff} = 0.13$ and $\mu_{cr} = 53\ \text{cm}^2.\text{V}^{-1}\text{s}^{-1}$. These calculated values are represented in the $(L_g{n_c}^{-1/4}; L_c{n_c}^{-1/3})$ plane with a grey-scale/color-mobility correspondence. The experimental Hall mobility data are represented in the same plane by circles whose tone/color gives the mobility value. (b) Analysis of the relative contribution of the three different mechanisms responsible for the carrier scattering phenomenon (defined as μ/μ_i) for three different FTO specimen of different thickness (A: 30 nm, B: 160 nm, and C: 440 nm).

$(L_g n_c^{-1/4}; L_c n_c^{-1/3})$ space using a color-mobility correspondence. The experimental data are shown with circles whose color indicates the experimental Hall mobility value. Figure 7(a) exhibits a rather good agreement between experimental and calculated values as the tone/color of figure background follows the tone/color of circles. In order to compare the relative contribution of the three different mechanisms, the relative importance of each scattering phenomenon i was defined as μ/μ_i and is plotted in Figure 7(b) for three FTO specimens A, B, and C whose thickness is 30, 160, and 440 nm, respectively. The mechanism which has the lowest mobility has the strongest influence on the total electron mobility in the film. For sample A (thinnest layer), the GB scattering is the dominant mechanism. For higher carrier mobility (like for the thickest sample C), the main scattering mechanism contribution is related to the ingrain one. This latter is mostly due to ionized impurities and to a lesser extent to phonons. Sample C corresponds to larger values of L_c and L_g compared with samples B and A.

It appears that for the three samples A, B, and C, twin boundaries have rather small effects on electron mobility. The two main scattering mechanisms are then related to the contribution of ingrain and grain-boundary. To compare these two effects, one can remove the calculated contribution arising from twin boundaries to the total mobility and plot this reduced mobility versus $L_g n_c^{-1/4}$ (proportional to μ_{GB}) as reported in Figure 8. The dashed and dotted-dashed curves are associated with GB and ingrain contributions, respectively. The continuous curve corresponds to the calculation of this reduced mobility while experimental values are represented by circles. The model show good agreement with experimental data. In Figure 8, the influence of fitting parameters can directly be assessed. Indeed, γ_{eff} determines the slope of the GB contribution (dashed curve) and μ_{cr} fixes the constant value of ingrain contribution (dotted-dashed curve). As the combination of these two diffusion mechanisms within the Matthiessen law gives the reduced mobility (i.e., continuous curve), the fitting parameters shape the asymptotic behavior of the reduced mobility at $L_g n_c^{-1/4} \to 0$ and $L_g n_c^{-1/4} \to \infty$. It should be noted that for the highly doped sample $(2 \times 10^{20}\,\text{cm}^{-3} < n_c < 4.6 \times 10^{20}\,\text{cm}^{-3})$ $L_g n_c^{-1/4}$ values are mainly dependent upon L_g variations. For samples having low $L_g n_c^{-1/4}$ values (small grains), the mobility is mainly limited by grain boundaries since $\mu_{GB} < \mu_{cr}$. On the contrary, specimens having large $L_g n_c^{-1/4}$ values (large grains) have mobility mostly limited by the ingrain scattering and as a consequence mobility is improved in comparison with FTO having small grain.

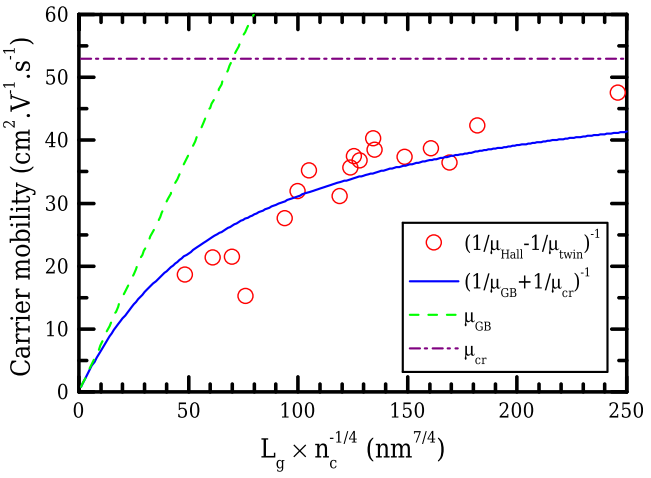

FIG. 8. Reduced mobility of the free carriers versus $L_g n_c^{-1/4}$ for highly doped FTO samples. The circles correspond to experimental data from which the twin boundaries contribution has been removed. This allows to observe the effects of the two prevailing scattering mechanisms: grain boundary and ingrain, represented as dashed and dashed-doted curves, respectively. The continuous curve corresponds to the calculation of this reduced mobility, showing a good agreement with experimental reduced mobility.

In other words for highly doped FTO specimens, the extended defects (mainly GB and in a lesser extend twin boundaries) can reduce the carrier mobility when the defect density is high, i.e., when FTO thin film is composed of small grains. In the case of FTO suitable for solar cell applications (resistivity as low as 3.7×10^{-4} Ω cm and sheet resistance of 8 Ω/□), ingrain scatterings are the main source of carrier transport limitation with a relative contribution of about 2/3. For these high doped specimens, ingrain scatterings are due to ionized doping impurity for 80% and phonons for 20%.

IV. CONCLUSIVE REMARKS AND PERSPECTIVES

In conclusion, polycrystalline FTO thin films have been grown by ultrasonic spray pyrolysis on glass substrate. By varying growth conditions, several FTO specimens have been deposited and their structural, electrical, and optical properties have been investigated. Structural observations reveal the presence of extended structural defects, such as grain and twin boundaries. The former are always present in crystalline TCOs but the latter is mainly representative of the FTO specimens. The contribution of each physical mechanism involved in the electron scattering has been considered. An expression has been derived to predict the influence of each mechanism upon the carrier mobility with only two free parameters. A thorough comparison between experimental data and calculations has enabled to disentangle these different mechanisms whose relative importance is then deduced. As expected, extended structural defects play the major role for thin FTO layers and its relative importance continuously decreases when the specimen thickness is increased due to increase of both grain size and crystallite size. For thicker FTO films, the ingrain scattering prevails, and more particularly, ionized impurity scattering. Twin boundaries also play a role, but with lower consequences than grain boundaries. The predominance of grain boundary scattering or ionized impurity scattering is under debate for FTO and other TCOs, the present study show that in case of FTO, one or the other can prevail over the other it depends on the specimen structural properties and doping level.

Finally, the present investigation provides a contribution towards the better understanding the physical origins of any improvement in the electro-optical properties of FTO thin films.

As a consequence, the obtaining of FTO layer with appropriate electro-optical properties for integration in solar

cell requires both the stoichiometry and the microstructure growth control. We reported here FTO thin films, 440 nm-thick, that exhibit a sheet resistance of 8 Ω/□, while retaining good transmittance over the visible range (up to 86% including substrate effect). Such a thin FTO layer is well optimized for being integrated as the front electrode, for instance, in a ZnO based dye sensitized solar cell, as recently shown by our group.[53–55]

Finally, the present investigation provides a contribution towards the better understanding the physical origins of any improvement in the electro-optical properties of FTO thin films.

ACKNOWLEDGMENTS

This work has been supported by the French Research National Agency (ANR) through the program "Habitat Intelligent et Solaire Photovoltaïque" (under the project "ASYSCOL"—Contract No. ANR-08-HABISOL-002) and the Carnot Institute Energies du Futur under the project ET Nano (Contract No. 10B792020A). The authors would like to warmly thank B. Doisneau, G. Giusti, C. Jimenez, and H. Roussel for fruitful discussions as well as A. Bionaz, M. Jouvert, and A. Muthukumar for their help during specimen deposition.

[1]K. Ellmer, Nature Photon. **6**, 809 (2012).
[2]D. S. Ginley, H. Hosono, and D. C. Paine, *Handbook of Transparent Conductors* (Springer, 2010).
[3]E. Fortunato and R. Martins, Phys. Status Solidi RRL **5**, 336 (2011).
[4]N. Yamamoto, H. Makino, S. Osone, A. Ujihara, T. Ito, H. Hokari, T. Maruyama, and T. Yamamoto, Thin Solid Films **520**, 4131 (2012).
[5]A. Kumar and C. Zhou, ACS Nano **4**, 11 (2010).
[6]K. L. Chopra, S. Major, and D. K. Pandya, Thin Solid Films **102**, 1 (1983).
[7]R. G. Gordon, MRS Bull. **25**, 52 (2000).
[8]C. G. Granqvist, Sol. Energy Mater. Sol. Cells **91**, 1529 (2007).
[9]G. Sanon, R. Rup, and A. Mansingh, Phys. Rev. B **44**, 5672 (1991).
[10]A. Klein, C. Körber, A. Wachau, F. Säuberlich, Y. Gassenbauer, S. P. Harvey, D. E. Profit, and T. O. Mason, Materials **3**, 4892 (2010).
[11]X. D. Zhang, Y. Zhao, Y. T. Gao, F. Zhu, C. C. Wei, X. L. Chen, J. Sun, G. F. Hou, X. H. Geng, and S. Z. Xiong, J. Non-Cryst. Solids **352**, 1863 (2006).
[12]S. J. C. Irvine, D. A. Lamb, V. Barrioz, A. J. Clayton, W. S. M. Brooks, S. Rugen-Hankey, and G. Kartopu, Thin Solid Films **520**, 1167 (2011).
[13]H.-C. Lee and O. O. Park, Vacuum **75**, 275 (2004).
[14]M. W. J. Prins, K.-O. Grosse-Holtz, J. F. M. Cillessen, and L. F. Feiner, J. Appl. Phys. **83**, 888 (1998).
[15]K. M. Yu, M. A. Mayer, D. T. Speaks, H. He, R. Zhao, L. Hsu, S. S. Mao, E. E. Haller, and W. Walukiewicz, J. Appl. Phys. **111**, 123505 (2012).
[16]H. Y. Liu, V. Avrutin, N. Izyumskaya, Ü. Özgür, A. B. Yankovich, A. V. Kvit, P. M. Voyles, and H. Morkoç, J. Appl. Phys. **111**, 103713 (2012).
[17]C. Charpentier, P. Prod'homme, and P. Roca i Cabarrocas, Thin Solid Films **531**, 424 (2013).
[18]R. L. Petritz, Phys. Rev. **104**, 1508 (1956).
[19]J. Y. W. Seto, J. Appl. Phys. **46**, 5247 (1975).
[20]J. Bruneaux, H. Cachet, M. Froment, and A. Messad, Thin Solid Films **197**, 129 (1991).
[21]E. Conwell and V. F. Weisskopf, Phys. Rev. **77**, 388 (1950).
[22]H. Brooks, Phys. Rev. **83**, 868 (1951).
[23]R. Dingle, Philos. Mag. **46**, 831 (1955).
[24]T. Pisarkiewicz, K. Zakrzewska, and E. Leja, Thin Solid Films **174**, 217 (1989).
[25]T. Yamada, H. Makino, N. Yamamoto, and T. Yamamoto, J. Appl. Phys. **107**, 123534 (2010).
[26]K. Ellmer and R. Mientus, Thin Solid Films **516**, 4620 (2008).
[27]G. Rey, Ph.D. Thesis, Grenoble University, France, 2012.
[28]F. J. Ferrer, J. Gil-Rostra, A. Terriza, G. Rey, C. Jiménez, J. Garcia-Lopez, and F. Yubero, Nucl. Instrum. Methods Phys. Res. B **274**, 65 (2012).
[29]W. Sellmeier, Ann. Phys. Chem. **219**, 272 (1871).
[30]G. E. Jellison and F. A. Modine, Appl. Phys. Lett. **69**, 371 (1996); **69**, 2137 (1996).
[31]P. I. Rovira and R. W. Collins, J. Appl. Phys. **85**, 2015 (1999).
[32]H. Fujiwara and M. Kondo, Phys. Rev. B **71**, 75109 (2005).
[33]V. Consonni, G. Rey, H. Roussel, and D. Bellet, J. Appl. Phys. **111**, 33523 (2012).
[34]V. Consonni, G. Rey, H. Roussel, B. Doisneau, E. Blanquet, and D. Bellet, Acta Mater. **61**, 22 (2013).
[35]A. Messad, J. Bruneaux, H. Cachet, and M. Froment, J. Mater. Sci. **29**, 5095 (1994).
[36]C. V. Thompson, Annu. Rev. Mater. Sci. **30**, 159 (2000).
[37]G. Haacke, J. Appl. Phys. **47**, 4086 (1976).
[38]T. Fukano and T. Motohiro, Sol. Energy Mater. Sol. Cells **82**, 567 (2004).
[39]N. W. Ashcroft and N. D. Mermin, *Solid State Physics* (Thomson Learning, 1976).
[40]B. Stjerna and C. G. Granqvist, Appl. Phys. Lett. **57**, 1989 (1990).
[41]T. J. Coutts, J. Vac. Sci. Technol. A **18**, 2646 (2000).
[42]T. Minami, H. Sato, K. Ohashi, T. Tomofuji, and S. Takata, J. Cryst. Growth **117**, 370 (1992).
[43]K. Ellmer, J. Phys. D: Appl. Phys. **34**, 3097 (2001).
[44]J. Steinhauser, Appl. Phys. Lett. **90**, 142107 (2007).
[45]I. Volintiru, M. Creatore, and M. C. M. van de Sanden, J. Appl. Phys. **103**, 33704 (2008).
[46]T. Pisarkiewicz and A. Kolodziej, Phys. Status Solidi B **158**, K5 (1990).
[47]C. G. Fonstad and R. H. Rediker, J. Appl. Phys. **42**, 2911 (1971).
[48]R. Von Baltz and W. Escher, Phys. Status Solidi B **51**, 499 (1972).
[49]S. Belgacem and R. Bennaceur, Rev. Phys. Appl. **25**, 1245 (1990).
[50]R. Lipperheide, T. Weis, and U. Wille, J. Phys.: Condens. Matter **13**, 3347 (2001).
[51]R. A. Brown, Phys. Rev. **156**, 692 (1967).
[52]A. Messad, Ph.D. Thesis, Université Paris 7 Denis Diderot, France, 1993.
[53]N. Karst, G. Rey, B. Doisneau, H. Roussel, R. Deshayes, V. Consonni, C. Ternon, and D. Bellet, Mater. Sci. Eng. B **176**, 653 (2011).
[54]G. Rey, N. Karst, B. Doisneau, H. Roussel, P. Chaudouet, V. Consonni, C. Ternon, and D. Bellet, J. Renew. Sustain. Energy **3**, 59101 (2011).
[55]E. Puyoo, G. Rey, E. Appert, V. Consonni, and D. Bellet, Phys. Chem. C **116**, 18117 (2012).